www.advenergymat.de

Deposition of Horizontally Stacked Zn Crystals on Single Layer 1T-VSe₂ for Dendrite-Free Zn Metal Anodes

Yuyin Li, Hoilun Wong, Jun Wang, Weiliang Peng, Yidi Shen, Mengyang Xu, Qi An, Jang-Kyo Kim, Bin Yuan,* William A. Goddard III,* and Zhengtang Luo*

Owing to the moderate redox potential and high safety, Zn metal anodes have been garnering great attention. However, the poor reversibility and limited-service period caused by side reactions and dendrites hinder their applications. Here, a novel anode material consisting of a hexagonal 1T-Vanadium diselenide (1T-VSe₂) film on graphene is developed as a zincophilic template to epitaxially electrodeposit hexagonal closest packed Zn to replace the conventional metal substrates in Zn batteries. The 1T-VSe₂/ Zn anode induces a horizontally (002)-oriented plate-like Zn crystal deposition morphology instead of randomly oriented grains that prompts the compact Zn deposition. According to density functional theory calculations, the VSe₂ substrate exhibits a higher Zn adsorption (-0.54 eV) than the graphene (-0.38 eV) or neat Zn (-0.48 eV) counterparts, leading to the enhanced zincophilicity and a lower nucleation overpotential, in agreement with the experimental results. The force field-based molecular dynamics simulations visualize Zn nucleation and morphological evolution at the atomistic level. The rapid adatom diffusion on VSe2 leads to layer-by-layer Zn electrodeposits with higher fraction of the (002) facets to effectively prohibit dendrite formation. The symmetric cell with 1T-VSe₂/Zn delivers an ultra-stable cyclic life of 2500 h with 50 mV overpotential at 1 mA cm⁻² and 1 mAh cm⁻².

1. Introduction

In the quest for high-energy-density storage, much more powerful battery systems are required than the currently available devices can offer. While much efforts have been directed on lithium-ion batteries (LIBs), the progress is impeded by the constrained supply chain for raw materials and by safety concerns.[1] The Zn metal anode, which works effectively in aqueous rechargeable batteries, has stimulated great interest as a replacement for batteries that use flammable organic electrolytes such as ethylene carbonatebased organic solvents.^[2] Zn ion batteries (ZIBs) are promising candidates for a powerful battery system, with many advantages such as an outstanding theoretical specific capacity of 5855 mAh cm⁻³, a potential of -0.76 V, an excellent ionic conductivity, and superior safety.[3,4] Nevertheless, two major obstacles impede further applications of Zn anodes. The most detrimental issue is the formation of dendrites occurring during cycles, leading to

Y. Li, H. Wong, J. Wang, M. Xu, Z. Luo Department of Chemical and Biological Engineering Guangdong-Hong Kong-Macao Joint Laboratory for Intelligent Micro-Nano Optoelectronic Technology William Mong Institute of Nano Science and Technology and Hong Kong Branch of Chinese National Engineering Research Center for Tissue Restoration and Reconstruction The Hong Kong University of Science and Technology Kowloon, Hong Kong 999077, P. R. China E-mail: keztluo@ust.hk W. Peng, B. Yuan School of Materials Science and Engineering South China University of Technology Guangzhou 510640, P. R. China E-mail: apsheng@scut.edu.cn

The ORCID identification number(s) for the author(s) of this article

can be found under https://doi.org/10.1002/aenm.202202983.

Guangzhou 510640, P. R. China Y. Shen, Q. An Department of Materials Science and Engineering Iowa State University Ames, IA 50011, USA J.-K. Kim Department of Mechanical and Aerospace Engineering The Hong Kong University of Science and Technology Kowloon, Hong Kong 999077, P. R. China I.-K. Kim School of Mechanical and Manufacturing Engineering University of New South Wales Sydney, NSW 2052, Australia W. A. Goddard III Materials and Process Simulation Center (MSC) MC 139-74 California Institute of Technology Pasadena, CA 91125, USA E-mail: wag@caltech.edu

Key Laboratory of Advanced Energy Storage Materials

DOI: 10.1002/aenm.202202983

W. Peng, B. Yuan

of Guangdong Province

www.advancedsciencenews.com

www.advenergymat.de

16146840, 2022, 47, Downloaded from https://onlinelibrary.wiley.com/doi/10.1002/amm.202202983 by California Inst of Technology, Wiley Online Library on [2001/2023]. See the Terms and Conditions (https://onlinelibrary.wiley.com/terms-and-conditions) on Wiley Online Library for rules of use; OA articles are governed by the applicable Creative Commons Licenses

low Columbic efficiencies (CEs) and a short cell cycle lifespan. Zn dendrites are formed when Zn metal is deposited upon charging to create a rough surface due to the uneven distribution of zincates, which migrate to the tips of protuberances to relieve the concentration polarization. ^[5] The rough surface morphology and the dendrites generated can easily penetrate the separator, resulting in short-circuit failure and corrosion. In addition, zinc presents a more negative reduction potential than hydrogen in water-based electrolytes, where the hydrogen evolution reaction (HER) inevitably takes place on the anode, corroding the surface and consuming water. Moreover, the H₂ gas produced thereby causes the battery to be inflated and unstable. ^[6] The competition between zinc electroreduction and hydrogen evolution results in pH fluctuations in the battery cell, reducing the reversibility and stability of active Zn.

A compact homogeneous zinc surface is crucial for a high capacity and long cycle lifespan. Aiming to alleviate the problems mentioned above, a series of strategies have been proposed, including the structural design of zinc metal anodes, manipulation of the interface between electrode and electrolyte, and optimization of the electrolyte composition. [7-9] Undoubtedly, it is necessary to improve the mechanical and chemical stability of the electrode surface because it directly influences the anode/electrolyte interface environment, which can uniformize the Zn²⁺ flux and improve the deposition kinetics.^[10,11] It was shown previously that the Zn HCP crystal provided a more stable anisotropic lattice property than other metals with cubic lattice symmetry.[12,13] For example, Li metal forms needle-like dendrites, while Zn prefers to grow into plate-like crystals. The close correlation between the intrinsic crystal symmetry and electrodeposition morphology offers an opportunity to control initial nucleation and growth of Zn dendrites. It was shown that Zn anodes with prolonged exposure to (002) basal facets revealed sluggish electrochemistry and HER inhibition in sharp comparison with the (100) or (101) surfaces. [14] As such, a sheared-graphene functional substrate [15] with a relatively small lattice mismatch with Zn(002), was employed to facilitate Zn deposits to form a hexagon morphology with (002) orientation parallel to the substrate surface. As a result, a well-aligned epitaxial Zn electrodeposition interface was obtained, with the CE > 99% for over 1000 cycles. In addition to the lattice control of the substrate, adjusting the Zn anode surface with salts or other additives can effectively switch the crystal growth orientation of the zincate formed during galvanizing, resulting in a flattened or random plating. The Zn surface modified with cetyltrimethylammonium bromide (CTAB), polyethylene glycol (PEG-8000), sodium dodecyl sulfate (SDS), or thiourea (TU) [6,16] altered the zinc deposition behavior to form different crystal structures and surface microstructures. The Zn-CTAB induced a highly directional deposition of zinc along the (101) plane, forming myriads of zinc flakes perpendicular to the substrate. In contrast, the Zn-SDS promoted zinc deposition along the (002) plane, decreasing corrosion currents and forming a uniform and dense plating pattern that extends battery life beyond 1000 cycles.^[16] Another efficient method is introducing a functional overlayer to guide the Zn deposition. An in-situ ZnSe growth cultivator was exploited to regulate (002) formation at the initial stage, inhibiting dendrite initiation and HER.[17] The deposited Zn aided by the functional layer tends to grow parallel to the

current collector, leading to exceptional cyclic stability for up to 1530 h. The foregoing discussion signifies that the formation of the (002) texture horizontally aligned along the deposition surface would offer an ultimate approach for realizing dendrite-free Zn deposition. Finding a modification strategy for the Zn surface to simultaneously enhance corrosion tolerance and dendrite resistance is most important.

With the above background in mind, we herein introduce a two-dimensional (2D) 1T-Vanadium diselenide (1T-VSe₂) on functional layer on the Zn anode. The V element has been widely utilized in the cathode materials in ZIBs,[18] like $Na_3V_2(PO_4)_3$ [19] and phenylamine (PA)-intercalated VOPO₄·2H₂O,^[20] which can boost fast zinc-ion diffusion for the remarkably improved cycling stability. The zincophilic VSe₂ promotes adatom mobility to increase the fraction of close-packed (002) facets during the deposition process, which in turn changes the plate-like Zn deposition behavior from random to horizontal alignment, so as to constrain side reactions and Zn dendrite formation. As demonstrated by the highsolution transmission electron microscopy (HRTEM) and X-ray diffraction (XRD) analysis, zincates on VSe2 have a propensity to expose more (002) planes. The surface structure can be tuned by accelerating ion transport while prohibiting HER. The 1T-VSe₂ layer leads to a Zn atom adsorption energy larger than for pure Zn or graphene, according to the DFT calculations, which decreases the nucleation overpotential for high-quality Zn deposition. The MD simulations predict that during the Zn deposition process, the lower diffusion barrier on the VSe₂ overlayer than the Zn substrate counterpart results in an early phase transformation from amorphous Zn to a well-arranged (002) lattice pattern. The high diffusivity of the adatom observed in the mean square displacement (MSD) analysis facilitated the development of a smooth deposition surface. [21,22] The protective layer formed thereby can suppress the corrosion in the ZnSO₄ electrolyte while retarding HER side reactions during the potentiostatic sweep test. As a result, a planar and well-ordered Zn surface is created in the half cell test, and the VSe₂-coated Cu retains an outstanding CE > 99% for the initial 530 cycles. Moreover, the lifespan of the symmetric cell reaches up to 2500 cycles at a current density of 1 mA cm⁻² and an areal capacity of 1 mAh cm⁻². Precisely controlling the crystallographic features of the Zn with the help of a coated layer offers exciting opportunities for ZIBs. This work reveals a surface-orientation-dependent growth mechanism at both the atomistic scale and mesoscale, offering a practical approach to suppressing dendrites to achieve an unprecedented lifespan for ZIBs and other metal batteries.

2. Theoretical Calculations Section

2.1. Density Functional Theory (DFT) Calculations

We used the Vienna Ab initio Simulation Package (VASP) to perform DFT calculations. ^[23,24] The Projector Augmented Wave (PAW) pseudopotential was used to describe the ion-electron interaction in the calculation. The plane wave cut-off energy is 500 eV throughout all simulations. To study the adsorption between Zn and Zn or VSe₂, we used a 4×4 (002) Zn

www.advancedsciencenews.com

www.advenergymat.de

16146840, 2022, 47, Downloaded from https://onlinelibtary.wiley.com/doi/10.1002/aemm.202202983 by California Inst of Technology, Wiley Online Library on [2001/2023]. See the Terms and Condition of the Condition

ns) on Wiley Online Library for rules of use; OA articles are governed by the applicable Creative Commons License

(10.47 Å \times 10.47 Å) and a 3 \times 3 VSe₂ (9.88 Å \times 9.88 Å) supercell. The vacuum space in the z-axis we set is 20 Å. The k-points grid is $5 \times 5 \times 1$.^[25] The adsorption energy was calculated as in Equation (1)[26]

$$E_{\rm ads} = E_{\rm total} - E_{\rm slab} - E_{\rm Zn} \tag{1}$$

where E_{slab} refers to the energy of the substrate, VSe₂, and either (002) or (101) Zn. $E_{\rm Zn}$ is the energy of one Zn atom; and E_{total} is the energy after the Zn atom is adsorbed on the substrate. The VESTA software was used for 3D visualization.^[27]

2.2. Molecular Dynamics (MD) Simulations

To gain insight into the nucleation and crystallization process during Zn atom deposition, we performed MD simulations with a large model size of 24 nm \times 21 nm \times 10 nm with 50 000 Zn atoms distributed randomly above the Zn or VSe₂ substrate. For the deposition process simulation, we heat the system in a canonical (NVT) ensemble at 900 K, which offers sufficient driving force for nucleation, then we quench to 300 K at a rate of 1 K ps⁻¹ for 600 ps for deposition, followed by equilibration for 3 ns at room temperature. [28,29] The time step for the motion was set to 0.001ps during the whole simulation

process. A Nose-Hoover thermostat is used to control the temperature.

The force field for Zn–Zn is the Modified embedded-atom method (MEAM),[30] while the force field for V-Se is the threebody Stillinger-Weber potential proposed by the Jiang group.^[31] The interaction between Zn-V and Zn-Se was trained using DFT calculations with the Perdew-Burke-Ernzerhof (PBE) functional, [32] including the Grimme DFT-D3 correction [33] for the van der Waals (vdW) interaction between the VSe2 layer and a hexagon of 6 Zn atoms. For the MD calculations, we fitted a 12/6 Lennard-Jones (LJ) potential parameters to the DFT results.[34] More fitting details can be found in the Supporting Materials (Figures S3 and S4, Supporting Information). The platform to run MD is the Large-scale Atomic/Molecular Massively Parallel Simulator (LAMMPS).[35] The visualizations are implemented with the Open Visualization Tool (Ovito) software.[36]

3. Results and Discussion

3.1. Characterization of the VSe₂ Film

The synthesis process of a VSe₂ film on a graphene support is illustrated in Figure 1a. Briefly, GO is coated with a layer of PDA, which confines the V⁵⁺ ions through electrostatic interactions

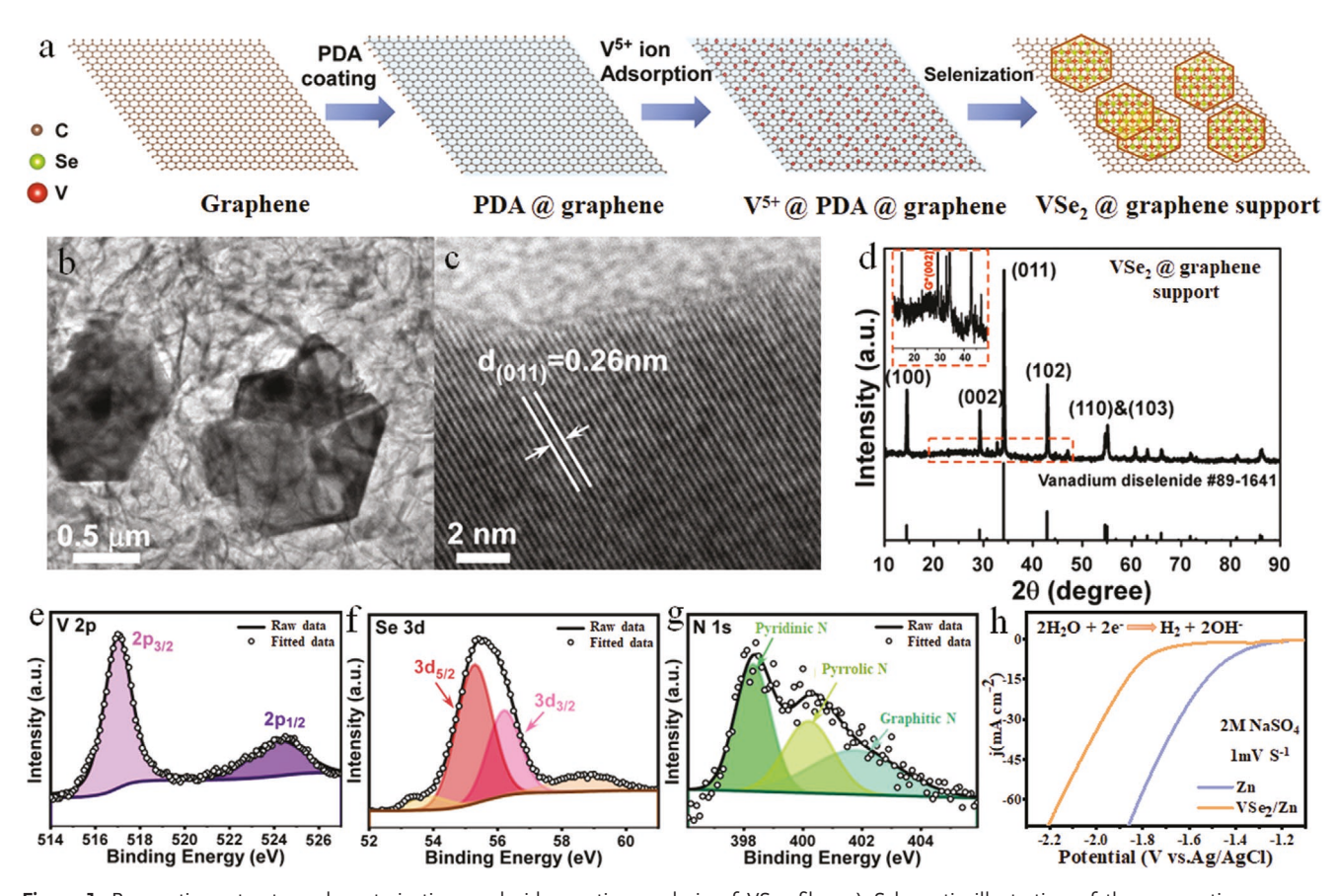


Figure 1. Preparation, structure characterization, and side reaction analysis of VSe2 film. a) Schematic illustration of the preparation process; b,c) HRTEM images; d) XRD pattern of VSe,; e-g) deconvoluted XPS spectra of V, Se, and N; and h) LSV curves of HER reactions for neat Zn and VSe₂/Zn in a 2 м aqueous Na₂SO₄ electrolyte at a scan rate of 1 mV s⁻¹.

IDVANCED

www.advenergymat.de

between VO₃⁻ and the amine groups from PDA. Subsequently, V⁵⁺@ PDA@graphene oxide is mixed with selenium and then selenized via CVD to fabricate the graphene-supported VSe₂. The morphology and structure of VSe₂ are characterized using a transmission electron microscope (TEM). We observed hexagonal-shaped single crystals of VSe₂ with a size of ≈1 µm, as shown in Figure 1b. The TEM image (Figure 1c) presents the inter-planer distance of 0.26 nm, matching with the (011) plane of VSe₂, in agreement with the previous literature. [18,37] The Energy dispersive analysis (EDS) of VSe2 is shown in Figure S5 (Supporting Information). The crystal structure of VSe₂ on the graphene support was analyzed by XRD as shown in Figure 1d. A broad diffraction peak at 25.3° is identified as the (002) plane of reduced graphene oxide. The distinct peaks observed at 14.6°, 29.3°, 34.3°, 43.0°, 54.7°, and 55.1° correspond to the (100), (002), (011), (102), (110), and (103) planes of VSe₂, respectively, confirming the VSe2 crystal structure. In addition, we studied the valence state of VSe₂ on the graphene support by X-ray photoelectron spectroscopy (XPS), confirming its elemental stoichiometry. High resolution 2p, 3d and 1s spectra of V, Se and N are displayed in Figure 1e-g, respectively. In the V 2p spectrum (Figure 1e), the peaks at 517.1 and 524.4 eV suggest the V 2p_{3/2} and V 2p_{1/2} orbitals, respectively.^[38] The divided peaks (Figure 1f) located at 55.3 and 56.2 eV in the Se 3d spectrum are associated with the Se $3d_{5/2}$ and Se $3d_{3/2}$ orbitals, respectively. [39] In Figure 1g, three kinds of nitrogen doping are identified from the peaks at 398.3 (pyridinic N), 400.2 (pyrrolic N) and 401.9 eV (graphitic N).[40] These foregoing observation confirmed the successful fabrication of graphene-supported VSe₂

To measure the reaction kinetics using VSe₂/Zn in the ZIBs, we carried out cyclic voltammetry (CV) tests using a threeelectrode system. For the electroreduction process, the Zn²⁺ ions were reduced instantaneously upon reaching the anode surface. The VSe2-coated Zn presented a larger reaction current density and a lower nucleation overpotential than the neat Zn electrode counterpart (Figure S6a, Supporting Information), indicating a faster ion diffusion and more rapid reaction kinetics of the VSe₂/Zn. The CV curves in the subsequent three cycles remain almost identical (Figure S6b, Supporting Information), suggesting a moderate surface environment during testing. The contact angle of the 2 M ZnSO₄ electrolyte on the VSe₂/Zn surface was 40.2°, much lower than that on the pure Zn surface (73.3°) (Figure S7, Supporting Information), indicating improved interfacial ion transfer. To study the undesirable HER side reaction, linear sweep voltammetry (LSV) test of the VSe₂/Zn anode was performed, finding a higher HER potential of 1.84 V than 1.47 V of the neat Zn anode. The digital photographs in Figure S8 (Supporting Information) present that many bubbles were formed on the Zn foil surface but not on the VSe₂/Zn electrode, indicating the resistance to the parasitic reactions and cyclic stabilization of the VSe2 film on the Zn anode surface.

3.2. (002) Plane-Oriented Zn Platelet Deposition on VSe₂ Film

The deposited Zn with abundant exposed (002) plane has been assumed to be favorable for enhanced corrosion resistance and

suppression of dendrite growth in the Zn anodes. [14] Although the Zn electrodeposits hold the same HCP-typed crystal lattice, the morphologies differ significantly when the deposition substrate varies. Principally, the Zn platelets tend to exhibit the (002) textured planes to minimize surface energy. However, irregularly distributed Zn deposits on a neat Zn reveal a random displacement of different grain orientations because of sluggish Zn mobility and formation of byproducts, as demonstrated in Figure 2a. By contrast, the high conductivity of VSe₂ with its superior Zn adatom self-diffusion enhances the fraction of (002) Zn lattice growth, giving rise to an alteration in deposition mode from random to horizontal stacking (Figure 2b). As a consequence, a dendrite-free deposition surface is required.

The morphologies of Zn on different substrates exhibited in SEM images of Figure 2c,d indicate that the deposited Zn on the commercial Zn substrate is disordered and irregular, where brutal pits and chips can penetrate the separator since the high Young's modulus of Zn ($E_{Zn} \approx 108$ GPa) compared with other anode metals. $^{[15]}$ But for the Zn coated on VSe_2 under the same conditions, we detected the horizontal stacking of platelets parallel to the VSe₂/Zn substrate (Figure 2e,f). The transection images exhibited in Figure S9a,b (Supporting Information), where the horizontally stacking Zn can also be clearly observed. With increasing the areal capacity to 5 mAh cm⁻², the denser and hexagon platelets can be found clearly above the VSe₂ functional overlayer (Figure S10, Supporting Information), indicating that 1T-VSe2 is important to regulate the hexagonal orientation and Zn deposition. The EDS elemental maps (Figure S11, Supporting Information) confirm that the deposited Zn indeed has a hexagonal shape.

The structure of Zn platelets on the VSe_2 cultivator was further confirmed by HRTEM and SAED. Figure 2g shows the deposited Zn hexagonal single crystal platelet. As illustrated in Figure 2h, we found the highlighted diffraction pattern of [100], [110] and [2 $\overline{1}0$]. All of these planes are oriented perpendicular to the (002) plane (inset in Figure 2h), signifying that the exposed hexagonal platelet in Figure 2g grows predominately along the (002) facet. The VSe_2 film is vital to accelerate the Zn growth mainly in the (002) plane, leading to dense and aligned platelike Zn deposition, beneficial for a desirable electrode/electrolyte interface.

To probe the textural change during the above electrochemical deposition process, ex situ XRD was taken after different deposition times and relative texture coefficient $RTC_{(hkl)}$ was calculated based on the XRD results. Figure 2i suggests that the Zn crystal on the VSe₂ surface is quite pure with negligible impurities. This means that the whole deposition process is reversible with high corrosion resistance. The Zn deposited on the VSe₂ surface recorded the highest (002) peak intensity after 40 min. We investigated the crystal orientation quantitatively at different deposition times by applying $RTC_{(hkl)}$ according to formula (2)^[11]

$$RTC_{(hkl)} = \frac{I_{hkl}/I_{hkl}^0}{\sum I_{hkl}/I_{hkl}^0} \times 100\%$$
 (2)

where I_{hkl} and I_{hkl}^0 are the intensities of (hkl) lines for the deposited Zn and the corresponding intensities of the standard Zn. Conceptually, when RTC_(hkl) \geq 20%, we may perceive the

16146840, 2022, 47, Downloaded from https://onlinelibrary.wiley.com/doi/10.1002/aenm.202202983 by California Inst of Technology, Wiley Online Library on [20/01/2023]. See the Terms and Conditions (https://onlinelibrary.wiley.com/term/

and-conditions) on Wiley Online Library for rules of use; OA articles are governed by the applicable Creative Commons

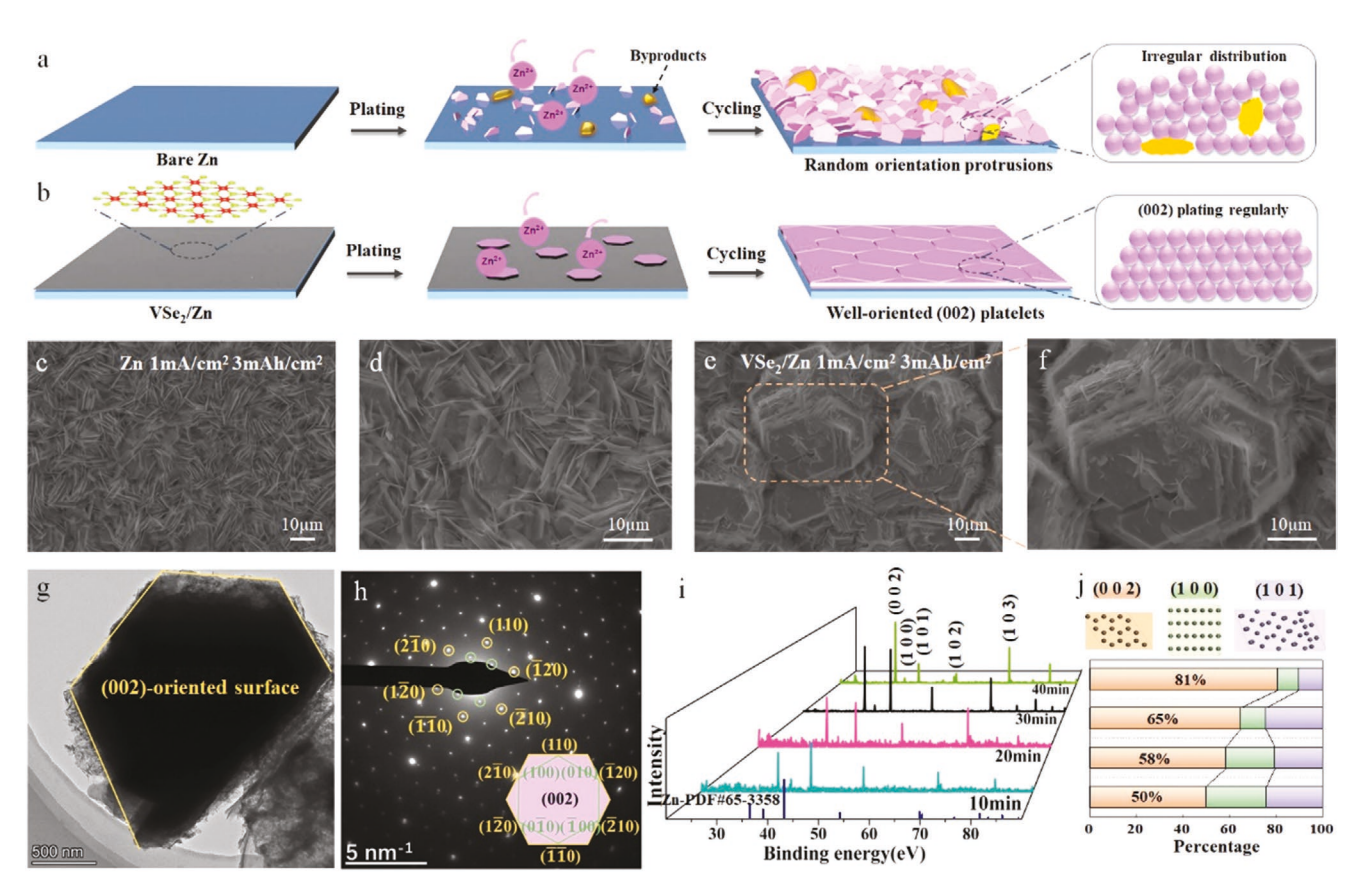


Figure 2. Deposition mechanism explanation with VSe₂ film and corresponding deposited behavior. a,b) Effect of bare Zn and VSe₂-coated Zn on deposition morphology; SEM images for Zn depositing c) on neat Zn at 1 mA cm⁻² and 3mAh cm⁻² d) at a high larger magnification; e) on VSe₂/Zn f) and at a high magnification; g,h) HRTEM and SAED pattern for (002) preferred orientation Zn platelet; i) ex situ XRD patterns measured for different deposition times; j) relative texture coefficients for exposed planes. VSe₂-coated Zn enables more Zn (002) to be exposed.

privileged orientation is (hkl), while the preferential orientation is absolute when the RTC_(hkl) value approaches 100%. At the beginning of 10 min deposition, the RTC(002) is 50%, for the longer deposition time of 20 min, it changes to 58%, and at 40 min, the percentage of the (002) plane increases up to 81%. This means that Zn on VSe₂ undergoes a reorientation transition during the continuous reduction $(RTC_{(002)}$ for pure Zn is 46%),^[12] indicating more (002) basal planes are exposed and more hexagonal Zn crystals are formed. The RTC for the (002) orientation on VSe₂ substrate is much higher than other planes, such as (100) and (101) (Figure 2j). The crystalline structure of graphene-like VSe2 possesses a similar hexagonal lattice pattern. VSe₂ layer imposes a lower diffusion barrier while boosting the adsorption energy as will be discussed in the next section. Therefore, Zn platelets with a high fraction of (002) facets are deposited parallel to one another on the VSe₂ surface, as observed in the SEM and HRTEM images (Figure 2c-h), which contributes to better electrochemical performance.

3.3. Revealing the Interaction Mechanism between Zn and VSe₂

The interaction mechanisms occurring between Zn and VSe_2 is probed through DFT and MD simulations systematically. The DFT results (Figure 3a) indicate that the Zn atom on VSe_2 has

stronger adsorption (-0.53 eV) than the neat Zn (-0.48 eV) and the graphene substrate (-0.38 eV), revealing the better zincophilicity of VSe₂ and a lower Zn (002) facet surface energy on VSe₂. This finding further confirms the low nucleation overpotential of the anode made therefrom during the CV test. Eventually, it will result in favorable platelet-like (002) Zn crystal deposition. In addition, the Bader charge analysis (Figure 3b) also confirms the strongest affiliation between VSe₂ and Zn, where 0.18 e are transferred from Zn to VSe₂ with the largest polarization amongst the three substrates studied. Owing to the favorable affinity, the Zn deposit avoids aggregation on the VSe₂ surface, suppressing the generation of Zn dendrites.

We performed the MD simulations to reveal the early polymorph evolution and crystallization process of Zn atoms at an atomistic scale. Figure 3c,e shows the starting configurations of random Zn (pink sphere) above the neat Zn (blue sphere) and the VSe₂ matrix (V: red; Se: green). After quenching and minimizing, the Zn atoms deposited on these two substrates show contrasting morphologies. The Zn deposited on the pure Zn is prone to accumulate together and distribute randomly (Figure 3d), whereas the Zn atoms prefer to grow layer by layer with a well-oriented growth direction on the VSe₂ layer (Figure 3f) due to the zincophilicity between VSe₂ and Zn. The top views offer further insights into the different deposition behaviors. The first layer deposited on the neat Zn substrate

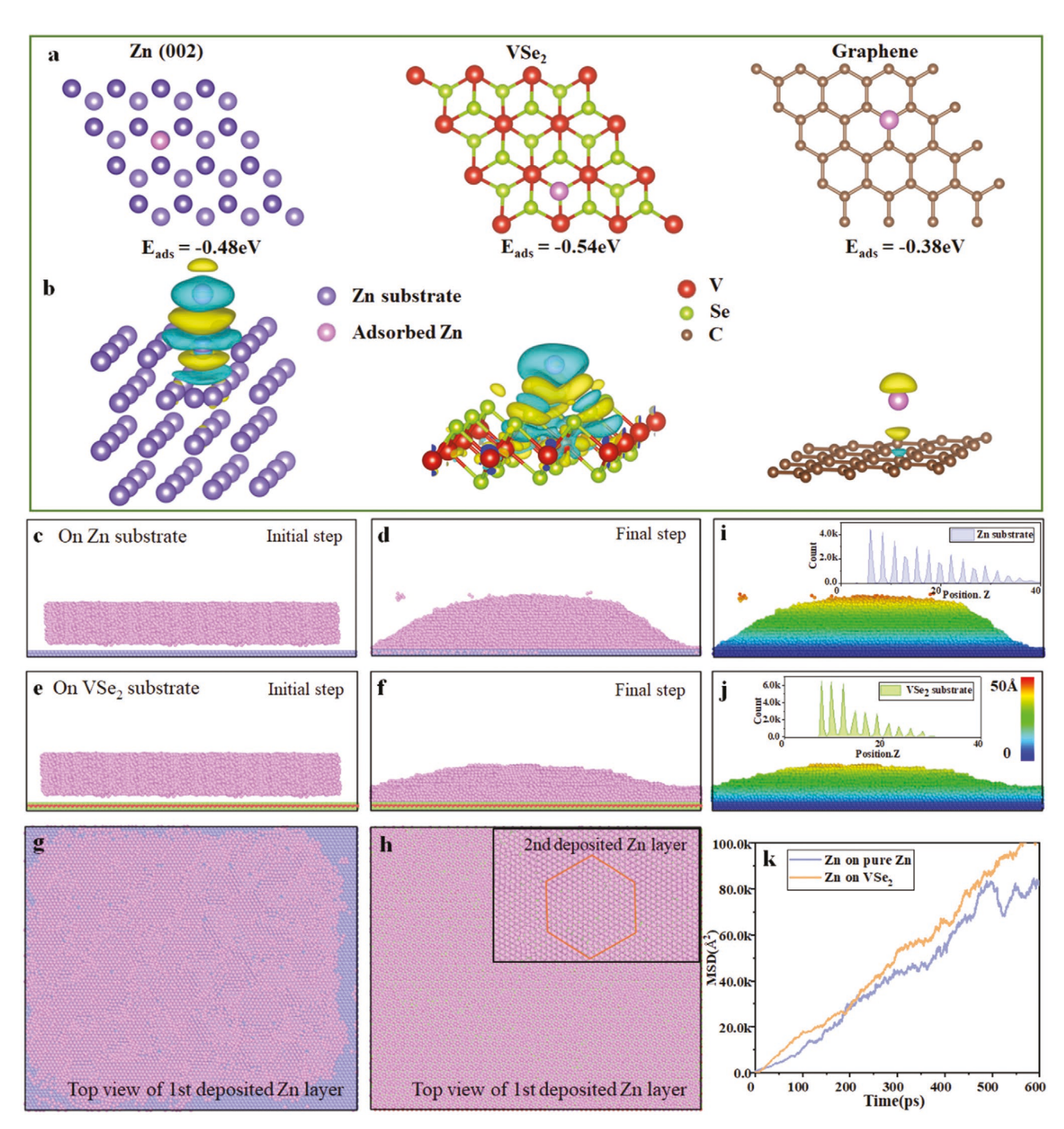


Figure 3. Computational results. a) Zn, VSe₂ and graphene models used in DFT calculations; b) Bader charge analysis; initial and final models for a Zn atom deposited c,d) on Zn substrate, and e,f) on VSe₂ substrate; Top view of the first Zn deposition layer g) on Zn substrate, h) on VSe₂ substrate, with the second layer showing hexagonal Zn crystal in inset; pink: adsorbed Zn; blue: Zn substrate; green: Se; red: V; brown: C. Final step of the surface roughness of the Zn deposit on i) Zn and j) VSe₂, with Zn atom distribution profiles along the Z-axis in inset; k) MSD results of Zn diffusion on neat Zn and VSe₂. Rapid surface transport plays a decisive role in the subsequence deposition behavior. Zn atoms prefer to grow layer by layer and show a well-oriented growth direction on VSe₂ substrate.

presents an uneven and bumpy surface with many cracks (Figure 3g). Upon further deposition, Zn atoms tend to gather randomly due to the "tip effect,"^[41] leading to the irregular deposition with a tendency toward the dendrite formation.^[42] In sharp contrast, the Zn atoms deposited on the VSe₂ surface are

atomically flat and fully covered (Figure 3h). Upon deposition of the second layer, Zn atoms tend to expose the most stable (002) plane (Inset figure in Figure 3h) because the (002) crystallographic orientation follows the tendency of energy minimization principle on the first formed smooth surface. These

16146840, 2022, 47, Downloaded from https://onlinelibrary.wiley.com/doi/10.1002/aenm.202202983 by California Inst of Technology, Wiley Online Library on [20/01/2023]. See the Terms

ns) on Wiley Online Library for rules of use; OA articles are governed by the applicable Creative Commons License

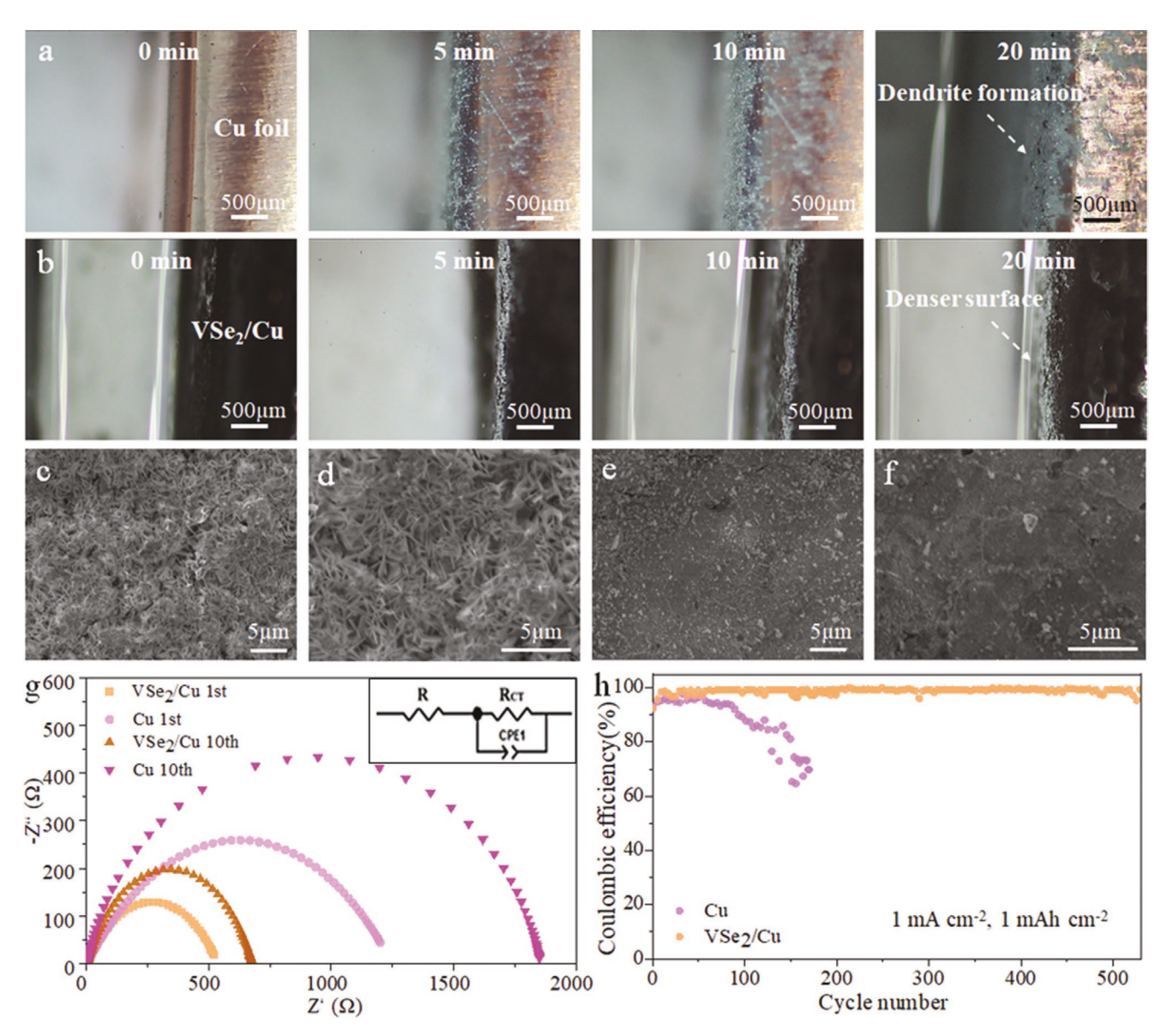


Figure 4. Deposition behavior of Zn in half cells. In situ optical microscope images of a) dendrite growth on bare Cu foil and b) denser surface of VSe₂/Cu foil; c,d) SEM images of Zn deposit on bare Cu foil; and e,f) on VSe₂/Cu foil half cells tested at 1 mA cm⁻² and 1 mAh cm⁻² for 10 cycles; g) Nyquist plots of Cu and VSe₂/Cu electrodes measured at 1 mA cm⁻² and 1 mAh cm⁻²; h) Coulombic efficiency obtained at 1 mA cm⁻² and 1 mAh cm⁻². VSe₂/Cu exhibits smoother and denser morphology after cycling and high Coulombic efficiency up to 99.0% for about 500 cycles.

simulation outcomes agree with the experimental observations employing TEM and XRD results in Figure 2h,i. Figure 3i,j shows the surface roughness of the deposition layer. There are apparent bulges on the Zn substrate with a deposition height beyond 50 Å, which is much higher than that on the VSe₂ substrate (39 Å). The additional (002) planes on VSe₂ lead to a smoother surface, which finally enhances the cycling stability of batteries. The inset figures show the Zn atom layer profile along the thickness direction of Z-axis. From the first to the third layer above VSe₂, each layer holds the same amount of Zn atoms with homogeneous distributions on the substrate, whereas those above the Zn substrate present continuously diminishing Zn atoms. This means that the VSe₂ film exerts a positive effect on Zn nucleation and growth at the initial stage

of deposition. The mean square displacement (MSD), which is proportional to the atom diffusion coefficient, is also measured to study the adatom mobility. Figure 3k demonstrates that the diffusion coefficient on VSe₂ is generally higher than that on the Zn substrate over the whole time studied. According to Davidson's model, the excellent adatom self-diffusivity contributes to a homogeneous electrodeposition morphology with a planar surface. Summarizing, it is demonstrated that the Zn surface transport characteristic plays a decisive role in the deposition behavior and the sluggish reaction kinetics on Zn is overcome by the VSe₂ functional film.

We assembled Zn||Cu and $Zn||VSe_2/Cu$ half cells to evaluate the reversibility of Zn deposition on each of the substrate. First, the real-time Zn deposition and dendrite growth are visualized

ADVANCED ENERGY MATERIALS

www.advancedsciencenews.com

www.advenergymat.de

by the in situ optical microscopy observations using transparent cells. As depicted in Figure 4a,b where the half cells are tested at a current density of 5 mA cm⁻², the neat Cu or VSe₂/Cu surface is shown at their original states. As time goes by, numerous protrusions in the form of Zn dendrites start to appear on the bare Cu surface, whereas the VSe₂/Cu surface remains largely intact. When the deposition time reaches 20 min, a significant difference between the deposits on the Cu and VSe₂/Cu electrode was detected. The VSe₂/Cu electrode affords a compact Zn surface without apparent projections. What's more, the SEM images of Zn deposits on the bare Cu foil obtained after 10 cycles at a current density of 1 mA cm⁻² exhibit a random, moss-like feature (Figure 4c), the magnification image can be seen in Figure 4d. However, a densely packed, planer surface was revealed on VSe2/Cu (Figure 4e,f). The rapid diffusion of Zn and a high zincophilic characteristic of VSe₂ are responsible for the uniform distribution and dramatically decreased dendrite formation. The EIS test results are fitted to the equivalent circuit to represent the charge transfer resistance ($R_{\rm CT}$) of the anode surface, as shown in Figure 4g. [45] After the first cycle, the $R_{\rm CT}$ of Cu is 1232.5 Ω , which is quite larger than that of VSe₂/ Cu electrode (514.1 Ω). A similar observation is noted even after 10th cycle: the surface impedance boosts significantly for Cu (1845.5 Ω for Cu) due to the HER side reaction and the surface roughness increase whereas the surface impedance of VSe₂/Cu electrode remains suppressed to 701.2 Ω , indicating ameliorated charge transfer and rapid diffusion kinetics on the surface. Besides, Figure S12 (Supporting Information) depicts the representative voltages curves of the cells with bare Cu and VSe₂/Cu electrodes, respectively. The cell with bare Cu electrode displays a larger voltage gap (165.6 mV) of a poor plating kinetics after 100 cycles than that of VSe₂/Cu cell (53.2 mV), primarily due to the dendrite formation and side reactions during repeated cycling. The Coulombic efficiencies (CEs) of the planar Cu and VSe₂/Cu cells to measure the ability for reversibility are shown in Figure 4h. The Cu foil electrode retains a stable CE of 98% in the initial 50 cycles at a current density of 1 mA cm⁻², but suffers a drastic deterioration of CE below 80% after 100 cycles. In comparison, the VSe₂/Cu electrode preserves a remarkably steady CE exceeding 99.0% for up to 530 cycles, which is attributed to the protective VSe₂ overlayer. The zincates appear not to be easily separated from the electrode, reducing the potential creation of "dead Zn." In summarizing, the rapid ion transfer, high adatom diffusivity and inhibition of side reactions aides by VSe₂ effectively prohibit the formation of dendrites to create a dense and uniform plating surface.

To thoroughly examine the electrochemical performance and energy storage ability using the VSe $_2$ /Zn electrode, the symmetric cells and full cells assembled with a α -MnO $_2$ cathode were tested using a 2 M ZnSO $_4$ electrolyte. Remarkably, under 1 mA cm $^{-2}$ and 1mAh cm $^{-2}$ testing conditions, the cell with VSe $_2$ /Zn maintains an exceptionally stable charge/discharge process for 2500 h without voltage variation (Figure 5a). In contrast, the cell prepared with nonmodified Zn electrode ran for \approx 320 h. The inset figure shows the voltage fluctuations of both cells from the 125th to 150th cycles. It is obvious that the symmetric cells containing a VSe $_2$ /Zn anode show a much smaller and more stable polarization overpotential for Zn deposition than the neat Zn, suggesting much better wettability of the

former. In particular, upon plating/striping cycles at a higher current density of 2 mA cm⁻² (Figure S13, Supporting Information), the VSe₂/Zn cell remains stable for over 1000 h, much longer than 245 h for the pristine Zn cell. The excellent cyclic performance of the former cell indicates that the VSe2-coated Zn benefits for the layer-by-layer planar Zn deposition morphology without further dendrite growth. Attaining a smooth deposition surface helps ensure a prolonged cycle time without short-circuiting the battery. The discharge capacities and corresponding CEs of the full cells were measured at a gravimetric current density of 1 A g⁻¹, as shown in Figure 5b. The capacity of VSe₂/Zn || a-MnO₂ cell after the first cycle is 195 mAh g⁻¹ with a remarkable retention rate of 94.7% after 500 cycles, which is much better than those of the Zn anode counterpart. Figure 5c shows the intrinsically steady capacity discharge process of the VSe₂/Zn || a-MnO₂ full cell. Figure 5d compares the cycling performance of symmetric Zn battery between our work and other state-of-the-art works with functional coatings, where the lifespan of the symmetric cells prepared with VSe₂/Zn outperformed the most studies. In addition, pouch cells were cycled to verify the application potential of the electrode materials. The cycling performance is shown in Figure 5e, where the pouch cell with VSe₂/Zn || a-MnO₂ displays a high capacity with retention of 83.2% after 150 cycles. The inset photo displayed the working states of full cell to lighten an indicator. The outstanding performance unveils the important function of the VSe2 cultivator, leading to fast ion transfer and adatom self-diffusivity conducive to the dendrite-free anode.

4. Conclusions

In summary, we developed a graphene-like 2D VSe2 cultivator as a coating on the Zn surface via a CVD method. With this functional layer, the deposited Zn tends to expose the (002) crystallographic planes and stacks parallel to the VSe₂/Zn electrode due to improved adatom mobility and high adsorption, as verified by the DFT and MD simulations. The high fraction of Zn (002) planes oriented horizontally with the VSe₂ layer leads to a smooth and uniform deposition surface. Moreover, the Zn corrosion induced by HER which otherwise presents on the neat Zn surface is also prevented by the VSe2 film. As a result, a compact and dendrite-free Zn interface is realized even after repeated cycles. The half cell prepared with a VSe₂/Zn electrode preserves a remarkably steady CE exceeding 99.0% for 530 cycles. The symmetric cell maintains an equally stable charge/ discharge process for 2500 h with negligible voltage variations. This work offers a simple yet rational approach to overcome the issue of parasitic reactions and dendrite growth, while providing insights into the mechanism behind the design of high-performance Zn metal batteries based on the theoretical simulation methods.

5. Experimental Section

Synthesis of the VSe₂ Layer: Graphene oxide (GO) was prepared by a modified Hummers method^[46,47] and used as the growth substrate for VSe₂. Then GO was dispersed into deionized (DI) water and mixed with 200 mg of dopamine, stirring for 30 min. Tris-HCl (100 mg) was added to

16146840, 2022, 47, Downloaded from https://onlinelibrary.wiley.com/doi/10.1002/aemm.202202983 by California Inst of Technology, Wiley Online Library on [20/01/2023]. See the Terms and Condition

und-conditions) on Wiley Online Library for rules of use; OA articles are governed by the applicable Creative Commons License

www.advancedsciencenews.com

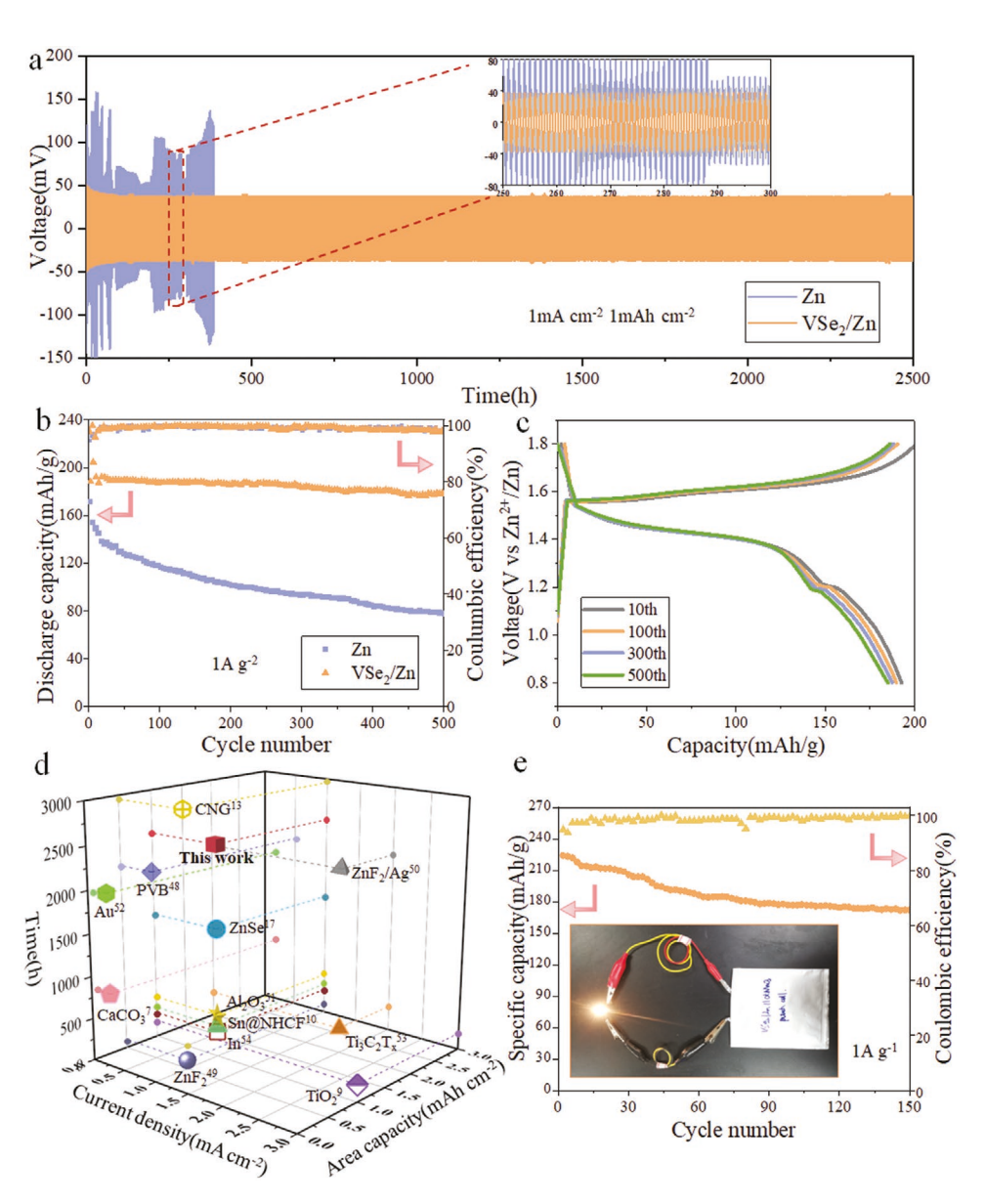


Figure 5. Electrochemical performance of symmetric cells and full cells. a) Cyclic performance of symmetric cells assembled from the neat Zn and VSe₂/Zn anode; b) long-term cyclic performance of ZIB full cells prepared with an α -MnO₂ cathode at 1 mA cm⁻² and 1 mAh cm⁻²; c) Charge/discharge curves at different cycles in ZIBs; d) Comparison of cycling stability of symmetric cells between this work and latest reported works with different coatings. e) Pouch cell electrochemical test result. Longer life span achieved by the VSe₂/Zn electrode, and 95% of capacity retention for the ZIBs after 500 cycles.

the dispersion and then stirring at 25 °C for 1 d. After the polymerization, polydopamine (PDA) with GO coating was washed with DI water by centrifugation at 15 000 rpm for 15 min each time and re-dispersed into DI water. Similar to the previous work, $^{[40]}$ 0.06 mmol of Ammonium metavanadate (NH $_4$ VO $_3$) was dropped in the re-dispersed GO solvent. After the freeze-drying, the sample was first annealed in the chemical vapor deposition (CVD) furnace at 300 °C for 1 h under 200 sccm Ar, then reacted with 20 mg of selenium powder at 500 °C for 30 min, with carrier gas of 10 sccm H $_2$ and 50 sccm Ar gases. The fabrication process of VSe $_2$ /Zn, VSe $_2$ /Cu and α -MnO $_2$ electrodes are summarized in Supporting materials (Figure S1a, Supporting Information), Figure S1b (Supporting Information) shows the digital photo of prepared VSe $_2$ /Zn electrode and Figure S2a (Supporting Information) shows the cross-section morphology of VSe $_2$ /Zn with the VSe $_2$ thickness of about 20 μ m. The Atomic force microscope (AFM) tests illustrate the height difference

of the coating is about 87.5 nm (Figure S2b, Supporting Information), indicating the surface of the VSe_2/Zn is relatively flat.

Material Characterization: Atomic force microscopy (AFM) [NanoScope IIIa/Dimension 3100 (Digital Instruments)] was used for surface roughness study. X-ray diffraction (XRD) was conducted to reveal the crystal lattice pattern of deposited Zn by Powder X-ray diffractometer_PANalytical equipment with 1.5406Å radiation. In addition, the elemental valence states and material composition were tested by X-ray photoelectron spectroscopy (XPS, PHI 5600 system). The deposition surface morphology and elemental composition were characterized via Scanning electron microscope (SEM, Super 40, Zeiss) and Energy dispersive analysis (EDS, XFlash Detector 5010, Bruker equipment). The High-resolution transmission electron microscope (HRTEM) was further used with selected-area diffraction (SAED) pattern to reveal the Zn atom deposition behavior. In situ dendrite growth

ADVANCED ENERGY MATERIALS

16146840, 2022, 47, Downloaded from https://onlinelibrary.wiley.com/doi/10.1002/amm.202202983 by California Inst of Technology, Wiley Online Library on [2001/2023]. See the Terms and Conditions (https://onlinelibrary.wiley.com/terms-and-conditions) on Wiley Online Library for rules of use; OA articles are governed by the applicable Creative Commons Licenses

www.advancedsciencenews.com www.advenergymat.de

process was observed on the Cu or VSe_2/Cu electrode surface using the in situ optical microscope analysis connected to the CT2001A test instrument. And the microstructure change during repeated cycles in the split cell was captured by an optical microscope.

Electrochemical Performance Test: CR2016-type cells with 2 M Zinc sulfate (ZnSO₄ · 7H₂O, Sigma) as electrolyte were constructed in an open environment for cyclic performance evaluation. Half cells with commercial Cu or VSe₂/Cu as the electrode and neat Zn as the anode were utilized to examine the reversibility capability. Then the symmetric cells Zn \parallel Zn and VSe₂/Zn \parallel VSe₂/Zn were assembled to test the cyclic capability. For the full cells, a-MnO2 was synthesized to use as the cathode materials on carbon cloth. The glass fiber film (420 μ m, Whatman GF/F) was used as the separator for all cells. For the pouch cells, the area of both electrodes is 8×8 cm2. The aforementioned α-MnO₂ slurry was coated on the carbon cloth and the mass loading is 2 mg cm⁻². The galvanostatic discharge-charge performance was obtained in the CT2001A test instrument (LAND Electronic Co, China). For the Hydrogen evolution reaction (HER) tests with a three-electrode system, The SI describes Electrochemical impedance spectroscopy (EIS) and cyclic voltammetry (CV) were operated in a CHI660e station.

Supporting Information

Supporting Information is available from the Wiley Online Library or from the author.

Acknowledgements

Y.L. and H.W. contributed equally to this work. Z.L. acknowledges support by the RGC (16304421), the Innovation and Technology Commission (ITC-CNERC14SC01), Guangdong Science and Technology Department (Project#:2020A0505090003), Research Fund of Guangdong-Hong Kong-Macao Joint Laboratory for Intelligent Micro-Nano Optoelectronic Technology (No. 2020B1212030010), IER foundation (HT-JD-CXY-201907), and Shenzhen Special Fund for Central Guiding the Local Science and Technology Development (2021Szvup136). Technical assistance from the Materials Characterization and Preparation Facilities of HKUST is greatly appreciated. W.A.G. acknowledges financial support by the US National Science Foundation (NSF CBET-2005250) and from the Hong Kong Quantum AI Lab Ltd. in the frame of the InnoHK initiative.

Conflict of Interest

The authors declare no conflict of interest.

Data Availability Statement

The data that support the findings of this study are available from the corresponding author upon reasonable request.

Keywords

dendrite suppression, molecular dynamics simulations, VSe_2 functional layers, zinc metal anodes

Received: August 31, 2022 Revised: September 28, 2022 Published online: October 31, 2022

- [3] L. E. Blanc, D. Kundu, L. F. Nazar, Joule 2020, 4, 771.
- [4] J. Hao, B. Li, X. Li, X. Zeng, S. Zhang, F. Yang, S. Liu, D. Li, C. Wu, Z. Guo, Adv. Mater. 2020, 32, 2003021.
- [5] W. Lu, C. Xie, H. Zhang, X. Li, ChemSusChem 2018, 11, 3996.
- [6] K. E. K. Sun, T. K. A. Hoang, T. N. L. Doan, Y. Yu, X. Zhu, Y. Tian, P. Chen, ACS Appl. Mater. Interfaces 2017, 9, 9681.
- [7] L. Kang, M. Cui, F. Jiang, Y. Gao, H. Luo, J. Liu, W. Liang, C. Zhi, Adv. Energy Mater. 2018, 8, 1801090.
- [8] Z. Zhao, J. Zhao, Z. Hu, J. Li, J. Li, Y. Zhang, C. Wang, G. Cui, Energy Environ. Sci. 2019, 12, 1938.
- [9] K. Zhao, C. Wang, Y. Yu, M. Yan, Q. Wei, P. He, Y. Dong, Z. Zhang, X. Wang, L. Mai, Adv. Mater. Interfaces 2018, 5, 1800848.
- [10] X. W. (David) Lou, L. Yu, D. Luan, L. Nian Wu, Y. Zeng, H. Yu, Sci. Adv. 2022, 8, eabm5766.
- [11] M. Shimizu, K. Hirahara, S. Arai, Phys. Chem. Chem. Phys. 2019, 21, 7045
- [12] K. S. Nagy, S. Kazemiabnavi, K. Thornton, D. J. Siegel, ACS Appl. Mater. Interfaces 2019, 11, 7954.
- [13] X. Zhang, J. Li, D. Liu, M. Liu, T. Zhou, K. Qi, L. Shi, Y. Zhu, Y. Qian, Energy Environ. Sci. 2021, 14, 3120.
- [14] M. Zhou, S. Guo, J. Li, X. Luo, Z. Liu, T. Zhang, X. Cao, M. Long, B. Lu, A. Pan, G. Fang, J. Zhou, S. Liang, Adv. Mater. 2021, 33, 2100187.
- [15] L. A. Archer, K. J. Takeuchi, D. C. Bock, L. Wang, Y. Deng, X. Liu, G. D. Renderos, C. D. Quilty, J. Yin, T. Tang, Q. Zhao, J. Zheng, A. C. Marschilok, E. S. Takeuchi, D. Zhang, C. Jaye, *Science* 2019, 366, 645.
- [16] X. Shi, G. Xu, S. Liang, C. Li, S. Guo, X. Xie, X. Ma, J. Zhou, ACS Sustainable Chem. Eng. 2019, 7, 17737.
- [17] X. Yang, C. Li, Z. Sun, S. Yang, Z. Shi, R. Huang, B. Liu, S. Li, Y. Wu, M. Wang, Y. Su, S. Dou, J. Sun, Adv. Mater. 2021, 33, 2105951.
- [18] Z. Wu, C. Lu, Y. Wang, L. Zhang, L. Jiang, W. Tian, C. Cai, Q. Gu, Z. Sun, L. Hu, Small 2020, 16, 2000698.
- [19] Z. Wu, F. Ye, Q. Liu, R. Pang, Y. Liu, L. Jiang, Z. Tang, L. Hu, Adv. Energy Mater. 2022, 12, 2200654.
- [20] L. Hu, Z. Wu, C. Lu, F. Ye, Q. Liu, Z. Sun, Energy Environ. Sci. 2021, 14, 4095.
- [21] D. Atkins, E. Ayerbe, A. Benayad, F. G. Capone, E. Capria, I. E. Castelli, I. Cekic-Laskovic, R. Ciria, L. Dudy, K. Edström, M. R. Johnson, H. Li, J. M. G. Lastra, M. L. De Souza, V. Meunier, M. Morcrette, H. Reichert, P. Simon, J. Rueff, J. Sottmann, W. Wenzel, A. Grimaud, Adv. Energy Mater. 2022, 12, 2102687.
- [22] J. Zheng, L. A. Archer, Sci. Adv. 2021, 7, eabe0219.
- [23] G. Kresse, J. Furthmüller, Comput. Mater. Sci. 1996, 6, 15.
- [24] G. Kresse, J. Furthmüller, Phys. Rev. B 1996, 54, 11169.
- [25] L. Yin, J. Liang, G. Zhou, F. Li, R. Saito, H. Cheng, Nano Energy 2016. 25, 203.
- [26] X. Gao, Q. Zhou, J. Wang, L. Xu, W. Zeng, Nanomaterials 2020, 10, 299.
- [27] K. Momma, F. Izumi, J. Appl. Crystallogr. 2008, 41, 653.
- [28] X. Wang, G. Pawar, Y. Li, X. Ren, M. Zhang, B. Lu, A. Banerjee, P. Liu, E. J. Dufek, J. Zhang, J. Xiao, J. Liu, Y. S. Meng, B. Liaw, *Nat. Mater.* 2020, 19, 1339.
- [29] M. Yang, Y. Mo, Angew. Chem., Int. Ed. 2021, 60, 21494.
- [30] H. Jang, K. Kim, B. Lee, CALPHAD 2018, 60, 200.
- [31] J.-W. Jiang, Parameterization of Stillinger-Weber potential for twodimensional atomic crystals, in Handbook of Stillinger-Weber Potential Parameters for Two-Dimensional Atomic Crystals, IntechOpen, Rijeka 2017, Ch. 1.
- [32] X. Xu, W. A. Goddard, J. Chem. Phys. 2004, 121, 4068.
- [33] S. Grimme, J. Antony, S. Ehrlich, H. Krieg, J. Chem. Phys. 2010, 132, 154104.
- [34] J. E. Jones, S. Chapman, Proc. R. Soc. London, Ser. A 1924, 106, 441.
- [35] A. P. Thompson, H. M. Aktulga, R. Berger, D. S. Bolintineanu, W. M. Brown, P. S. Crozier, P. J. in 't Veld, A. Kohlmeyer,

^[1] K. Du, E. H. Ang, X. Wu, Y. Liu, Energy Environ. Mater. 2021, https://doi.org/10.1002/eem2.12271.

^[2] H. Yan, X. Zhang, Z. Yang, M. Xia, C. Xu, Y. Liu, H. Yu, L. Zhang, J. Shu, Coord. Chem. Rev. 2022, 452, 214297.



ENERGY

16146840, 2022, 47, Downloaded from https://onlinelibrary.wiley.com/doi/10.1002/aemn.202202983 by California Inst of Technology, Wiley Online Library on [20/01/2023]. See the Terms

(https://onlinelibrary.wiley.

ons) on Wiley Online Library for rules of use; OA articles are governed by the applicable Creative Commons License

www.advancedsciencenews.com www.advenergymat.de

- S. G. Moore, T. D. Nguyen, R. Shan, M. J. Stevens, J. Tranchida, C. Trott, S. J. Plimpton, Comput. Phys. Commun. 2022, 271,
- [36] A. Stukowski, Modell. Simul. Mater. Sci. Eng. 2009, 18, 015012.
- [37] Y. Bai, H. Zhang, B. Xiang, X. Liang, J. Hao, C. Zhu, L. Yan, ACS Appl. Mater. Interfaces 2021, 13, 23230.
- [38] Y. Yi, X. Du, Z. Zhao, Y. Liu, H. Guan, X. Liu, X. Pei, S. Zhang, D. Li, ACS Nano 2022, 16, 7772.
- [39] C. Wang, X. Wu, Y. Ma, G. Mu, Y. Li, C. Luo, H. Xu, Y. Zhang, J. Yang, X. Tang, J. Zhang, W. Bao, C. Duan, J. Mater. Chem. A 2018, 6, 8299.
- [40] H. Wong, X. Ou, M. Zhuang, Z. Liu, M. D. Hossain, Y. Cai, H. Liu, H. Lee, C. Wang, Z. Luo, ACS Appl. Mater. Interfaces 2019, 11, 19986.
- [41] L. Enze, J. Phys. D 1986, 19, 1.
- [42] D. A. Cogswell, Phys. Rev. E: Stat., Nonlinear, Soft Matter Phys. 2015, 92, 011301.
- [43] S. J. Banik, R. Akolkar, J. Electrochem. Soc. 2013, 160, D519.
- [44] R. Davidson, A. Verma, D. Santos, F. Hao, C. Fincher, S. Xiang, J. Van Buskirk, K. Xie, M. Pharr, P. P. Mukherjee, S. Banerjee, ACS Energy Lett. 2019, 4, 375.

- [45] M. Idrees, S. M. Abbas, Ata-Ur-Rehman, N. Ahmad, M. W. Mushtaq, R. A. Naqvi, K. Nam, B. Muhammad, Z. Iqbal, Chem. Eng. J. 2017, *327*, 361.
- [46] W. S. Hummers, R. E. Offeman, J. Am. Chem. Soc. 1958, 80, 1339.
- [47] Z. Luo, Y. Lu, L. A. Somers, A. T. C. Johnson, J. Am. Chem. Soc. 2009, 131, 898.
- [48] J. Hao, X. Li, S. Zhang, F. Yang, X. Zeng, S. Zhang, G. Bo, C. Wang, Z. Guo, Adv. Funct. Mater. 2020, 30, 2001263.
- [49] H. Qiu, X. Du, J. Zhao, Y. Wang, J. Ju, Z. Chen, Z. Hu, D. Yan, X. Zhou, G. Cui, Nat. Commun. 2019, 10, 5374.
- [50] D. Wang, D. Lv, H. Peng, N. Wang, H. Liu, J. Yang, Y. Qian, Nano Lett. 2022, 22, 1750.
- [51] H. He, H. Tong, X. Song, X. Song, J. Liu, J. Mater. Chem. A 2020, 8, 7836.
- [52] M. Cui, Y. Xiao, L. Kang, W. Du, Y. Gao, X. Sun, Y. Zhou, X. Li, H. Li, F. Jiang, C. Zhi, ACS Appl. Energy Mater. 2019, 2, 6490.
- [53] Y. Tian, Y. An, C. Wei, B. Xi, S. Xiong, J. Feng, Y. Qian, ACS Nano 2019, 13, 11676.
- [54] K. Hu, X. Guan, R. Lv, G. Li, Z. Hu, L. Ren, A. Wang, X. Liu, J. Luo, Chem. Eng. J. 2020, 396, 125363.